d-electron contribution to the stopping power of transition metals

J. P. Peralta,* A. M. P. Mendez, D. M. Mitnik, and C. C. Montanari
Instituto de Astronomía y Física del Espacio, CONICET and Universidad de Buenos Aires, Buenos Aires 1428, Argentina

(Received 14 November 2024; accepted 26 February 2025; published 11 March 2025)

We present a nonperturbative model to describe the stopping power by ionization of the *d* electrons of transition metals. These metals are characterized by the filling of the *d* subshell and the promotion of some of the electrons to the conduction band. The contribution of *d* electrons at low-impact energies has been noted experimentally in the past as a break of the linear dependence of the stopping power with the ion velocity. In this paper we describe the response of these electrons considering the atomic inhomogeneous momentum distribution. We focus on the transition metals of groups 10 and 11 in the Periodic Table: Ni, Pd, Pt, Cu, Ag, and Au. Results are shown to describe the low-energy stopping power, with good agreement with the experimental data and available time-dependent density-functional theory results. By combining the present nonperturbative model for the *d*-subshell contribution with other approaches for the valence electrons and for the inner shells, we provide a coherent theoretical method capable of describing the stopping power of these transition metals from the very-low- to the high-energy region.

DOI: 10.1103/PhysRevA.111.032808

I. INTRODUCTION

Following the IUPAC principles of chemical nomenclature [1], a transition metal is any element of groups 3–12 of the Periodic Table, also known as the *d*-block elements. Their electronic configuration is $ns^{k-j} + (n-1)d^j$, with n the main quantum number, k the group number, and j the number of d electrons. In the literature (see, e.g., [1] and references therein), there is a discussion about whether group 12 (Zn, Cd, and Hg) is a transition metal because of its filled *d* subshell, i.e., s^2d^{10}, and the related chemical characteristics. For example, for the solids of group 12, the experimental *d* binding energy has been measured (being $E_d \sim 10$ eV in all the cases [2]); however, for solids of groups 3–11, this value is still under discussion. The binding energy is an important quantity of the partially filled *d* metals, which strongly impacts the electronic energy loss.

For the earlier transition metals ($k = 3$–7), the maximum oxidation state is k [1], i.e., all the *d* and *s* electrons may be valence electrons. In a solid, all these k electrons belong to the conduction band and are well described by the free-electron gas (FEG) model [3]. The Seitz radius r_S of these elements also have experimental and theoretical values agreeing within 5%, which makes them canonical metals [4]. For the later transition metals ($k = 8$–11), the oxidation number is much smaller than k [1]. As solid metals, the number of electrons in the FEG is not k either: *d* electrons are partially promoted to the FEG and the rest remain bound. The number of *d* electrons in the conduction band, the number of bound electrons, and the value of the binding energy E_d are very relevant and still open subjects.

The energy loss in the later transition metals has been the subject of multiple experimental [5–18] and theoretical studies [19–26]. These works were guided not only by their well-known properties and applications but also by some specific findings about low-energy stopping power and the response of *d* electrons. At very low energies, the FEG approximations suggest a linear dependence of the electronic stopping power with the ion velocity. For Cu, Ag, and Au (group 11), the experimental values showed an unexpected break of this linear behavior [5–14]. This has been attributed to the contribution of *d* electrons, as a drastic change in the r_S above a specific critical impact velocity [7]. Surprisingly, the low-energy stopping power of Ni, Pd, and Pt (group 10) does not show the mentioned change in slope [13–17].

Perhaps the most detailed *ab initio* theory for stopping power calculations is the time-dependent density-functional theory (TDDFT) [27]. This theory accurately describes the low-energy stopping power, being more suitable for channeling or monocrystalline targets than for polycrystalline or amorphous ones (off-channeling). However, including all (or most of) the target electrons to extend the stopping power to intermediate and high impact energies represents a heavy task. Recent TDDFT results for stopping power in Fe, Ni, Cu, Pt, and Au [21–26] show a soft nonlinearity rather than the mentioned broken line and change in slope.

In this work we present a nonperturbative model for calculating the *d*-electron contribution to the electronic stopping power in the later transition metals. The goal of this contribution is to describe the experimental values at low impact energies but also the total electronic stopping power in an extended energy range. We focus on groups 10 and 11, i.e., Ni, Pd, Pt, Cu, Ag, and Au, due to the different low-energy behaviors experimentally found. We aim to understand and describe the physics involved in the response of these weakly bound *d* electrons to the ion passage. The present results are

*Contact author: jpperalta@iafe.uba.ar

compared with the experimental compilation in the IAEA electronic stopping power database [28,29], highlighting the most recent low-energy experimental data [6–18]. We also collate our curves with the available TDDFT (off-channeling) results [22–25]. By means of the independent shell approximation, we are able to predict the total electronic stopping power by combining our model results for the d-electron contribution with those corresponding to nonperturbative [4] and perturbative FEG models [30] and the shellwise local plasma approximation with Levine-Mermin dielectric function (SLPA-LM) for the deeply bound shells [31,32]. The present results focus on the low-energy region and the dependence of the stopping power on the impact velocity and also cover the extended energy range up to 100 MeV.

The theoretical proposal is introduced in Sec. II. The present results and the comparison with the available experimental measurements are displayed and analyzed in Sec. III. A summary and discussion of our conclusions are given in Sec. IV. Atomic units are used throughout this work unless specified otherwise.

II. THEORETICAL MODEL

Let us consider a point charge moving with velocity v in a cloud of d electrons with an inhomogeneous velocity profile and a momentum distribution function $f(p)$. The electronic stopping cross section $S(v)$ is given by [33,34]

$$S(v) = \frac{2}{(2\pi)^3}\int \mathrm{d}\vec{p}\, f(p) v_r \frac{\vec{v}_r\cdot\vec{v}}{v}\sigma_{tr}(v_r), \tag{1}$$

where $\vec{v}_r = \vec{v} - \vec{p}$ is the relative velocity, $\vec{p}$ is the electron momentum, which is equivalent to the electron velocity in atomic units, $\sigma_{\rm tr}(v_r)$ is the transport cross section

$$\sigma_{\rm tr}(k) = \frac{4\pi}{k^2}\sum_{l=0}^{\infty}(l+1)\sin^2[\delta_l(k)-\delta_{l+1}(k)], \tag{2}$$

and $\delta_l(k)$ are the phase shifts generated by a central potential $V(r)$ of the projectile screened by the d electrons. In the present proposal, we consider the velocity-dependent screened potential introduced in Ref. [4], which verifies the cusp condition for the induced density around the charged projectile. This characteristic proved decisive for low-energy antiproton stopping power [4].

By writing $v_r = (v^2 + p^2 - 2vp\cos\varphi)^{1/2}$, invoking $d\vec{p} = 2\pi p^2 dp \sin\varphi\, d\varphi$, and changing the integration variable from φ to v_r, Eq. (1) can be expressed as

$$S(v) = \frac{1}{(2\pi v)^2}\int_0^{\infty} dp\, p\, f(p) I(p), \tag{3}$$

with

$$I(p) = \int_{|v-p|}^{|v+p|} dv_r v_r^2\left(v_r^2 + v^2 - p^2\right)\sigma_{\rm tr}(v_r). \tag{4}$$

A change of the order of the integrals in Eqs. (3) and (4) gives

$$S(v) = \frac{1}{(2\pi v)^2}\int_0^{\infty} dv_r v_r^2 \sigma_{\rm tr}(v_r) I'(v_r), \tag{5}$$

with

$$I'(v_r) = \int_{|v_r-v|}^{|v_r+v|}\left(v_r^2 + v^2 - p^2\right) p\, f(p) dp. \tag{6}$$

This change locates the distribution function in the inner integral and the transport cross section in the outer one, improving the performance of the numerical calculations of the stopping cross sections.

In the present model we propose to describe the response of d electrons through an inhomogeneous momentum distribution function given by

$$f_{nl}(p) = \frac{(2\pi)^3}{2}|\Phi_{nl}(\vec{p})|^2, \tag{7}$$

with $\Phi_{nl}(\vec{p})$ the Fourier transform of the wave functions $\phi_{nl}(\vec{r})$, normalized to the number of electrons N_e in the nl subshell. With this definition, the distribution function $f_{nl}(p)$ verifies

$$\int f_{nl}(p) d\vec{p} = \frac{(2\pi)^3}{2} N_e. \tag{8}$$

In the homogeneous FEG model [33], the momentum distribution function is given by a step function within the Fermi sphere, $f_{\rm FEG}(p) = \Theta(p - p_F)$, where p_F is the Fermi momentum and

$$\int \Theta(p - p_F) d\vec{p} = \frac{(2\pi)^3}{2} n_e, \tag{9}$$

with n_e the density of electrons, $n_e = N_{\rm FEG} n_{\rm at}$, $N_{\rm FEG}$ is the number of electron in the FEG, and $n_{\rm at}$ is the atomic density. The difference between Eqs. (8) and (9) is the difference between stopping cross section and energy loss per unit path length.

Within this model, given by Eqs. (5)–(7), we analyze the contribution to the stopping power of the $3d$, $4d$, and $5d$ subshells of Ni, Cu, Pd, Ag, Pt, and Au, as applicable. The transport cross section in Eq. (5) was calculated by numerically solving the Schrödinger radial equation for the free states of the electrons in a central potential $V(r)$ [35]. We used the potential proposed in [4], with a screening density $N_e n_{\rm at}$.

The wave functions in Eq. (7) for Ni and Cu are the nonrelativistic Hartree-Fock results by Bunge *et al.* [36], while for Pd, Ag, Pt, and Au we solved the fully relativistic atomic structure using the HULLAC code package [37,38] (for more details, see Ref. [39]). As expected, the binding energies for the lowest charged Ni and Cu obtained from the nonrelativistic Hartree-Fock method are in complete agreement with the relativistic HULLAC results.

The momentum distribution functions $f_{nl}(p)$ given by Eq. (7) were obtained analytically by expanding the wave functions $\phi_{nl}(r)$ in a Slater function. Considering this expansion, the Fourier transform of the Slater functions is analytical using Flannery-Levy integrals [40]. Then the integration in Eq. (6) is also analytical (see the Appendix for details).

III. RESULTS

In Table I we tabulated the details about the transition metals studied here. These metals have loosely bound d electrons. Some of them are promoted to the conduction band, while

TABLE I. Atomic structure, valence, and d electrons of Ni, Cu, Pd, Ag, Pt, and Au. The outer electrons of the electronic configuration are shared, $N_{\rm FEG}$ electrons are in the FEG, and N_d electrons remain in the d subshell. Here r_S is the Wigner-Seitz radii, ω_p is the plasmon frequency, and E_F is the Fermi energy. Also included are the experimental values for the plasmon peak $\omega_p^{\rm expt}$ and the dump value $\gamma_p^{\rm expt}$ obtained from [41]. In addition, E_d, v_d, and $\langle r_d \rangle$ are the theoretical binding energy, mean velocity, and mean ratio of the atomic d subshell, respectively, from Hartree-Fock [36] (Ni and Cu) and full relativistic calculations [39] (Pd, Pt, Ag, and Au). Atomic units are used.

		Atomic	FEG						d bound			
Element	Z	configuration	$N_{\rm FEG}$	r_S	ω_p	$\omega_p^{\rm expt}$	$\gamma_p^{\rm expt}$	E_F	N_d	E_d	$\langle v_d \rangle$	$\langle r_d \rangle$
						Group 10						
Ni	28	[Ar] $3d^8 4s^2$	3	1.80	0.714	0.716	0.27	0.564	7	0.707	3.72	0.965
Pd	46	[Kr] $4d^{10}$	7	1.50	0.942	0.937	0.21	0.815	3	0.216	2.60	1.61
Pt	78	[Xe] $5d^9 6s^1$	7	1.51	0.929	0.919	0.17	0.801	3	0.250	2.45	1.71
						Group 11						
Cu	29	[Ar] $3d^{10} 4s^1$	3	1.85	0.689	0.707	0.29	0.537	8	0.491	3.73	0.991
Ag	47	[Kr] $4d^{10} 5s^1$	3	2.09	0.572	0.625	0.20	0.420	8	0.641	2.88	1.37
Au	79	[Xe] $5d^{10} 6s^1$	7	1.57	0.877	0.864	0.53	0.742	4	0.309	2.67	1.58

others remain bound to the target nucleus. Knowing how many d electrons are part of the FEG and how many remain bound is crucial to the energy-loss description. To this end, we analyzed data from reflection electron energy-loss spectroscopy in solids by Werner *et al.* [41]. The experimental plasmon frequency $\omega_p^{\rm expt}$ and dump $\gamma_p^{\rm expt}$ in Table I were obtained from the first significant peak and width of the energy-loss function in Ref. [41]. From $\omega_p^{\rm expt}$, the number of electrons in the FEG can be inferred. In the present calculations, we consider $N_{\rm FEG}$ as the integer number that is closest to that value. The plasmon frequency ω_p, the Wigner-Seitz radii r_S, and the Fermi energy E_F in Table I are obtained from these $N_{\rm FEG}$ values.

The atomic configuration and characteristics of the d bound electrons in the columns on the right in Table I are the result of the Hartree-Fock (Ni and Cu) and the fully relativistic atomic structure calculations (Pd, Ag, Pt, and Au) [37–39]. It is important to note that these values correspond to the atoms, not to the solid targets. This distinction is evident when comparing the values of E_F and E_d (the atomic binding energy of the d electrons) displayed in Table I. Assuming that some of the d electrons are promoted to the FEG, the remaining ones must have $E_d > E_F$. According to the values shown in Table I, $E_d \ll E_F$ for Pd, Pt, and Au, which suggests that for these targets, most of the loosely bound d electrons are transferred to the FEG. Instead, in Ni, Cu, and Ag, only one or two d electrons are promoted to the conduction band. For solid Cu, Ag, and Au, density of states calculations with density-functional theory [42] are such that $0.05 \leqslant E_d - E_F \leqslant 0.15$. For Ni and Pt, the difference in energy between the d electrons and the Fermi energy is even more minor.

In Fig. 1 we display the inhomogeneous momentum distribution functions $f_{nd}(p)$ given by Eq. (7) for the six targets studied here. We also include in this figure the homogeneous FEG distribution $f_{\rm FEG}(p)$. To compare them equivalently, we plotted $f_{nd}(p) n_{\rm at}$. The Heaviside function in $f_{\rm FEG}$ is constant and equal to 1, cutting off at p_F. Conversely, the $f_{nd}(p)$ distribution has a lower amplitude than the FEG one but extends far away from the Fermi sphere of the FEG and falls drastically within the Fermi region. For Pd, Pt, and Au, the value of v_d is smaller than for the others, which explains the maximum of their $f_{nd}(p)$ being shifted to lower values of p.

The total stopping cross section is obtained by adding all electronic contributions. At low impact energies, they are the FEG and the d-electron contributions. To extend the results to higher energies, even the deep shells should be added. In Sec. III A we present our low-energy results for Ni, Cu, Pd, Ag, Pt, and Au and in Sec. III B we extend the calculation to the high-energy region. For proton impact energies around the maximum and below, the experimental stopping power cross sections present considerable dispersion [29], and this spread is more notorious for the historically most measured targets (Au, Ag, Cu, and Ni). We consider all the experimental data available in Ref. [28]; however, we pay special attention to the most recent measurements at low energies, namely, those conducted from 1990 onward with $v \leqslant 1$. These values are highlighted in Figs. 2–13 with colors and closed symbols. The other low-energy experimental data, which were measured 35 or more years ago, are displayed altogether with half-closed circles, while the rest of the data in the database [28], i.e., the experiments at intermediate and high energies, are illustrated with open circles.

A. Low-energy stopping cross sections

In Figs. 2–7 we display the present theoretical stopping cross sections of the six targets studied here as a function of the impact velocity v, with $0 \leqslant v \leqslant 1$, and we compare them with the available experimental data compiled in [28]. The stopping due to the FEG is calculated as in Ref. [4]. It is worth noting that both the FEG and the d-electron models are nonperturbative. The FEG and d-electron contributions are shown separately, and the total stopping cross section results from adding both. The influence of the d-electron contribution to the stopping power is evident in all these figures.

The stopping power cross sections of H in Ni are shown in Fig. 2. The importance of the d contribution is remarkable above $v = 0.5$. The present results allow describing the experimental values in this energy region. The agreement with data in Refs. [15,16] is very good. We also include in Fig. 2 the

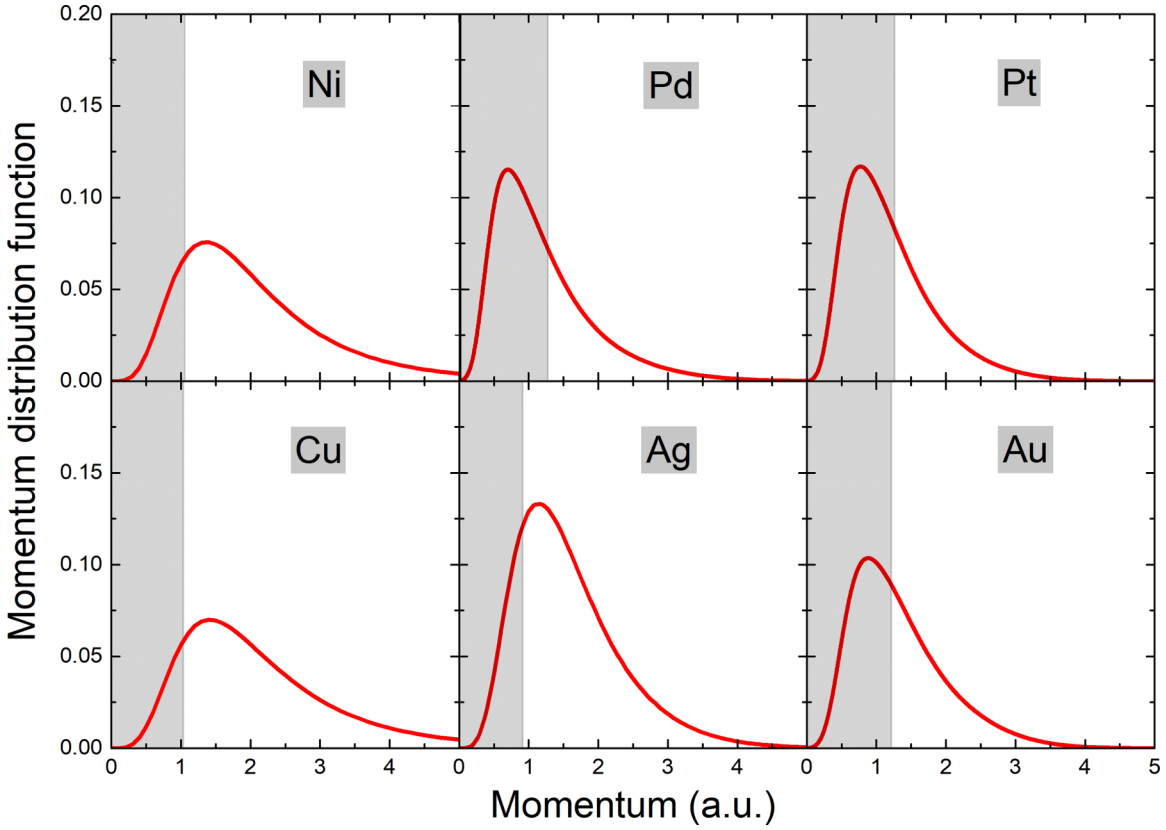

FIG. 1. Distribution functions of the d electrons, $f_{nd}(p)$, for the six targets considered here (red solid curve) and the FEG (light gray area from 0 to Fermi momentum).

TDDFT results by Quashie and Correa [23] for off-channeling Ni, with ten active electrons. The agreement between the present results and the TDDFT ones is excellent. We consider that the comparison of our results with the experimental data and a state-of-the-art model supports the present model.

In Fig. 3 we illustrate the case of H in Cu. The spread of experimental data in this region is significant. At very low impact velocities, there are two tendencies of the experimental values, where the backscattering measurements from Ref. [6]

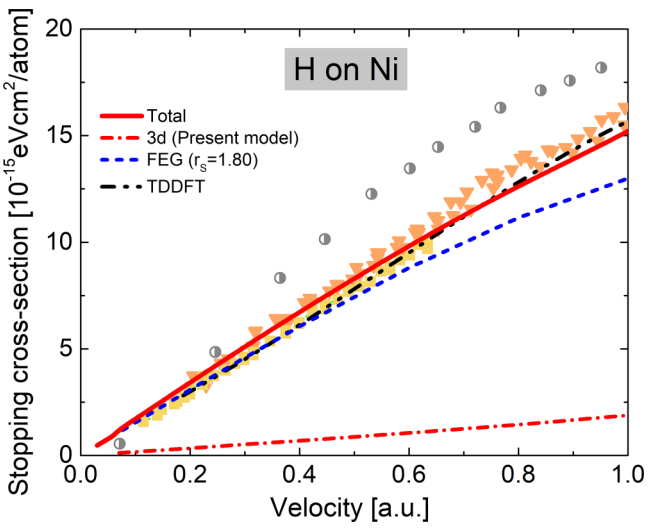

FIG. 2. Low-energy stopping cross section of Ni for H as a function of the impact velocity. Curves show the total stopping (red solid line), the present model for d-electron contributions (red dash-dotted line), the FEG stopping (blue dashed line), and the TDDFT results by Quashie *et al.* [23] (black dash–double-dotted line). Symbols, available experimental data: ▼, [15]; ■, [16]; and ◑, low-energy data in [28] before 1990.

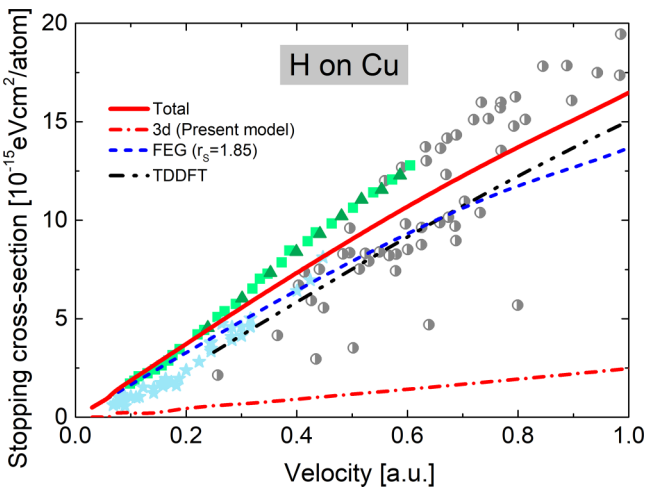

FIG. 3. Low-energy stopping cross section of Cu for H as a function of the impact velocity. Curves are the same as in Fig. 2, including the TDDFT results by Quashie and Correa [22]. Symbols, available experimental data: ★, [6]; ■, [7]; ▼, [8]; and ◑, data in [28] before 1990.

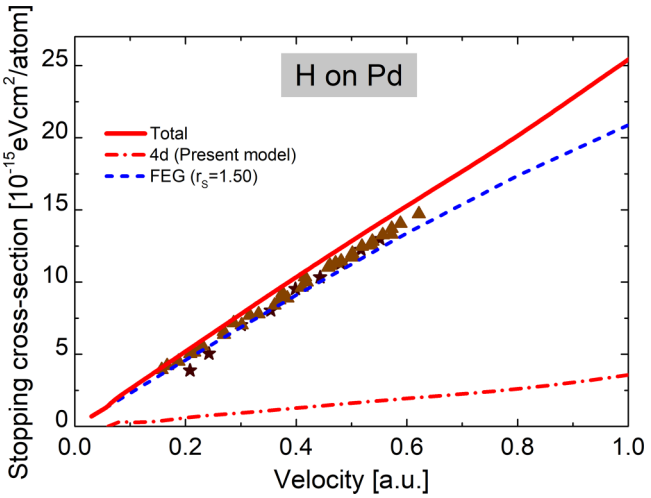

FIG. 4. Low-energy stopping cross section of Pd for H as a function of the impact velocity. Curves are the same as in Fig. 2. Symbols, available experimental data: ▲, [13]; and ★, [17].

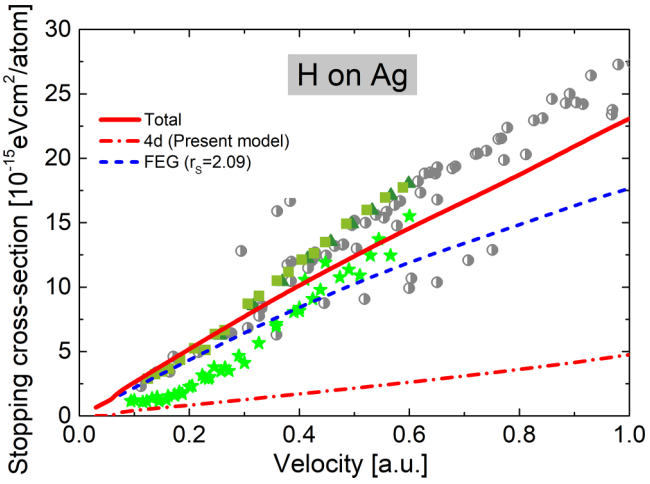

FIG. 5. Low-energy stopping cross section of Ag for H as a function of the impact velocity. Curves are the same as in Fig. 2. Symbols, available experimental data: ■, [7]; ★, [12]; ▲, [11]; and ◑, data in [28] before 1990.

are much lower than the transmission measurements from Refs. [7,8]. It can be noted that these two groups of data are supported separately by older measurements, specifically [43,44], respectively. Our total stopping cross sections, which add the FEG and the 3*d* contribution, agree with Ref. [7] at the lowest impact velocities and lie between both experimental data groups for $v > 0.3$. As in Fig. 2, we include the TDDFT values by Quashie and Correa [22]. Our results are close but above these values, which only agree with the measurements from Ref. [6] for $v < 0.3$. Our model for the *d*-electron contribution to the stopping power does not include an explicit threshold energy; it solely relies on the information of the inhomogeneous momentum distribution function. This missing feature may introduce some degree of overestimation at very low velocities.

The present results for H in Pd are displayed in Fig. 4. Only two data sets are available at low velocities, those in [13] and [17], which agree pretty well with each other and show an almost perfect linear dependence of the stopping power with the impact velocity. Our results describe these values quite well; the total stopping power is slightly higher than the experimental data, with differences that are less than 5%.

In Fig. 5 we display the case of H in Ag. Similarly to the Cu case, the experimental data are separated into two groups: The lower-lying data are backscattering measurements by Goebl *et al.* [12] and the higher-lying data are transmission measurements by Cantero *et al.* [7] and Valdés *et al.* [11]. The present total stopping results are closer to the higher experimental values from Ref. [7] for $v < 0.4$ and to the data from Ref. [12] for $0.4 < v \leqslant 0.6$. Our results show the importance of the *d*-subshell contribution above $v = 0.3$. As in the other cases, the present model does not describe the inclusion of *d* electrons in the total stopping power as a sharp change of slope in the linear velocity dependence but as a smooth difference between the FEG contribution and the total stopping values.

The present results for H in Pt are displayed in Fig. 6, together with the available data [12,14,18] and recent TDDFT values by Li *et al.* [24,25]. Our total values, considering the FEG and the 5*d* contributions, are slightly above these state-of-the-art values, but they are very close in amplitude. It is worth noting that the two experimental data sets for very low velocities [12,14] agree pretty well between with each other and neither of them indicates a break of the linear response at low energies. We also show in Fig. 6 our previous theoretical results, where we considered $N_{\mathrm{FEG}} = 10$, i.e., all *d* electrons are included in the FEG [32]. The difference is not significant, but it shows better overall agreement with the available experimental data. Nevertheless, we consider the present model to describe this group of targets more properly and in a more general way.

Finally, our results for H in Au are displayed in Fig. 7. This system features the most significant number of stopping power measurements with the broadest dispersion [28,29]. The present results agree with one group of data sets [11,17],

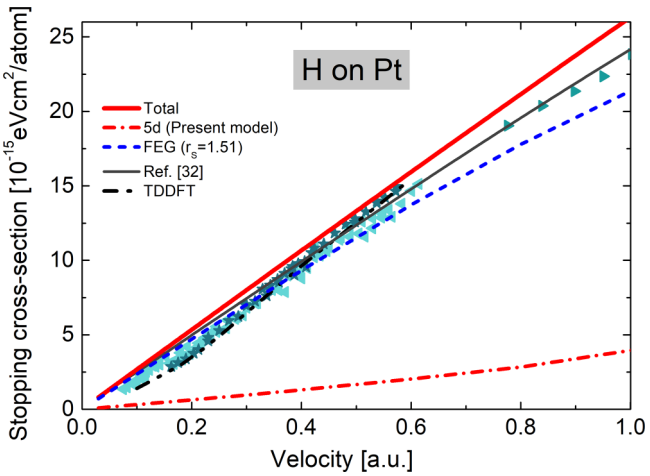

FIG. 6. Low-energy stopping cross section of Pt for H as a function of the impact velocity. Curves are the same as in Fig. 2, with the TDDFT results by Li *et al.* [25]; the dark gray solid line shows total values with all the *d* electrons in the FEG by Peralta *et al.* [32]. Symbols, available experimental data: ◄, [12]; ★, [14]; and ►, [18].

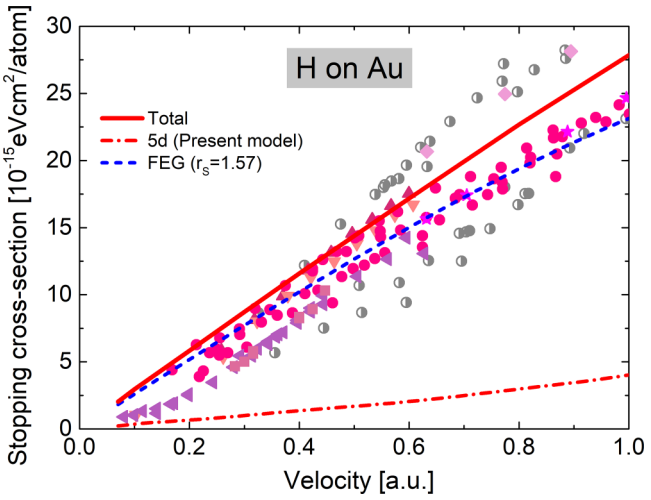

FIG. 7. Low-energy stopping cross section of Au for H as a function of the impact velocity. Curves are the same as in Fig. 4. Symbols, available experimental data: ○, [15]; ■, [6]; ▼, [17]; ▲, [11]; ★, [18]; ◀, [9]; ♦, [45]; and ◑, data in [28] before 1990.

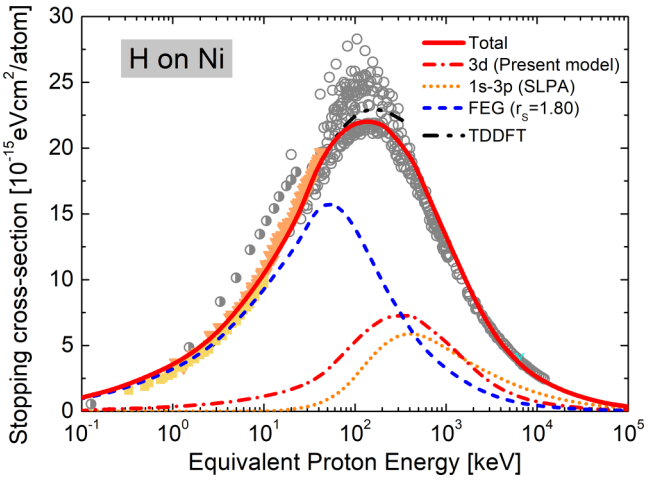

FIG. 8. Stopping cross section of Ni for H as a function of the impact energy. Curves show the total stopping (red solid line), the present model for d-electron contributions (red dash-dotted line), the FEG stopping (blue dashed line), the SLPA-LM values [32] for the inner shells (orange dotted line), and the TDDFT results by Quashie and Correa [23] (black dash–double-dotted line). Symbols are the same as in Fig. 2, as well as ◯ denoting the medium- to high-energy experimental data in [28].

while they overestimate other groups of measurements [6,9]. The low-energy measurements in these last measurements [6,9] are very close to channeling stopping values in Au ⟨100⟩ by Valdés *et al.* [5] and to the TDDFT results in Au ⟨100⟩ by Zeb *et al.* [21]. Time-dependent density-functional theory calculations for polycrystalline Au could bring some clarity to this case.

Considering the results in Figs. 2–7, we can say that there is a clear difference between the transition metals of groups 10 and 11. The change in the linear behavior with the impact velocity is not necessarily the most critical difference found in the cases examined here but rather the dispersion of experimental data, which is very important in group 11 and almost negligible in group 10. Our results agree with the measurements in metals from group 10 and somewhere in the middle of the data cloud of the metals from group 11. As already mentioned, we do not rule out a small overestimation at the lowest velocities shown here related to the energy threshold. This topic is a subject for future developments.

We thoroughly analyzed the values of $N_{\rm FEG}$ and N_d in the six cases studied here; nevertheless, we acknowledge they may be the subject of discussion. To further examine the present model along with the choice of these electron numbers, we extend the present results to intermediate to high energies and compare them with all the available data.

B. Stopping cross sections in an extended energy range

The energy loss in an extended energy range is displayed in Figs. 8–13. In these figures we present total and fully theoretical calculations, including SLPA-LM [32] values for inner-shell contributions. Above a certain impact velocity v_P, plasmon excitations of the FEG are relevant [46], where $v_P \simeq v_F(1+\sqrt{3\pi\, v_F})$, with v_F the Fermi velocity. We model the FEG contribution over a wide energy range using the nonperturbative model [4] for $v < v_P$ and the Mermin-Lindhard [30] results for the FEG for energies above that of plasmon excitation [3,4,32,47]. Then the present approach provides a coherent theoretical method capable of describing the stopping power from the very low (0.1 keV) to the high but not relativistic energy region (100 MeV). The whole picture given by Figs. 8–13 is promising. As already mentioned, the spread of experimental data around the stopping maximum characterizes the six targets, with Au, Ag, Cu, and Ni being the most striking cases.

For H in Ni, we display in Fig. 8 the extended energy version of the present calculations. In this figure the contribution of the $3d$ electrons and the $1s$ to $3p$ electrons is shown in the extended energy range. It can be noted that the $3d$ curve has a maximum at 350 keV/amu, where the ion velocity is close to the mean velocity of the $3d$ electrons, i.e., $v \simeq v_d$. Although there is a striking disparity of values, the stopping maximum of H in Ni has not been measured since 1986 [48]. Our total stopping cross section agrees very well with Ref. [15] and the data around the stopping maximum from Ref. [48]. The comparison with the TDDFT results by Quashie and Correa [23] (off-channeling and 16 active electrons) is very good. It is worth noting that the present model includes all target electrons (up to the K shell) by means of the SLPA-LM [32], allowing the description in the extended energy range shown in this figure.

The stopping cross sections for H in Cu as a function of the impact energy are displayed in Fig. 9. As mentioned for the case of Ni, the $3d$ contribution is maximum for $v \simeq v_d$. The present total stopping values are higher but in relatively good agreement with TDDFT results reported in Ref. [22]. For energies above 500 keV, the TDDFT curve underestimates the measurements due to the partial number of electrons considered. Again, the present agreement with the high-energy data is due to the inclusion of the $1s$ to $3p$ electrons contribution using the SLPA-LM.

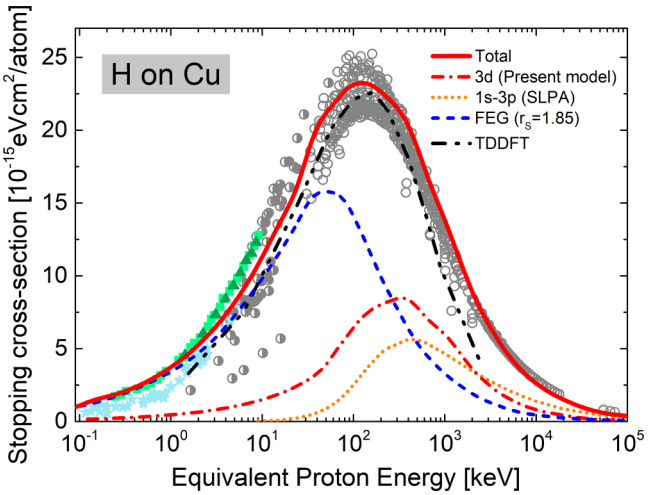

FIG. 9. Stopping cross section of Cu for H as a function of the impact energy. Curves are the same as in Fig. 8, with the TDDFT results by Quashie and Correa [22]. Symbols are the same as in Fig. 3, as well as ◯ denoting the experimental data in [28].

The results for H in Pd are presented in Fig. 10. This case differs from the previous ones: For impact energies above 100 keV, the stopping power due to the $1s$ to $4p$ subshells is higher than the $4d$-subshell contribution. The $4d$ electrons of Pd have lower mean velocities v_d than Ni and Cu (see Table I). This is consistent with a maximum of the d curve at lower energies ($E \sim 160$ keV). Our total values agree very well with the data at low and high energies, with the stopping maximum being close to the data [49]. The most recent measurements

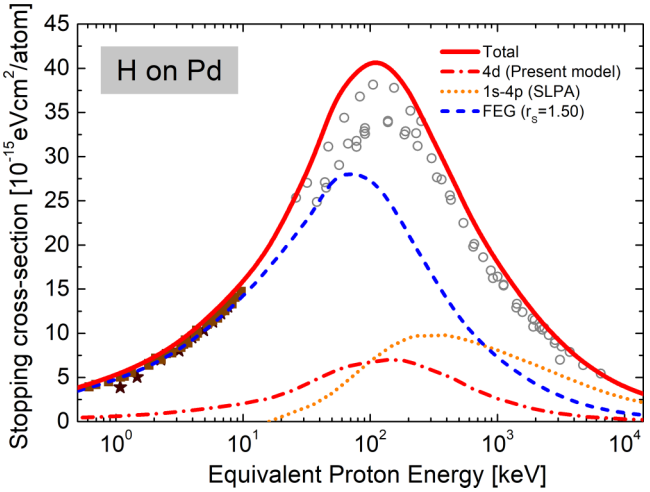

FIG. 10. Stopping cross section of Pd for H as a function of the impact energy. Curves show the total stopping (red solid line), the present model for d-electron contributions (red dashed line), the FEG stopping (blue dashed line), the SLPA-LM values [32] for the inner shells (orange dotted line), and the Mermin energy-loss function–generalized oscillator strength (MELF-GOS) results [51] (green dash–double-dotted line). Curves are the same as in Fig. 4; the dark gray solid curve is the SLPA-LM values [32] for the inner shells. Symbols are the same as in Fig. 4, as well as ◯ denoting the experimental data in [28].

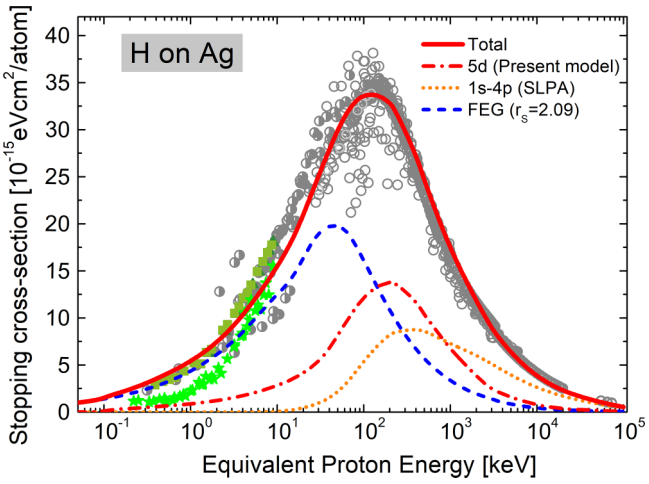

FIG. 11. Stopping cross section of Ag for H as a function of the impact energy. Curves show the total stopping (red solid line), the present model for d-electron contributions (red dash-dotted line), the FEG stopping (blue dashed line), and the SLPA-LM values [32] for the inner shells (orange dotted line). The symbols are the same as in Fig. 5, as well as ◯ denoting the experimental data in [28].

by Moro *et al.* [50] obtained a stopping maximum which is 15% below our result. Very recent perturbative results by Cheng *et al.* [51] based on the experimental energy-loss function and the MELF-GOS theory are also displayed in Fig. 10. These values describe the measurements above 70 keV and converge to our curve at high energies. In Fig. 11 we display the present stopping values of H in Ag. The agreement with the experimental data is good, considering the large dispersion of values. The present description of the d-electron contribution is crucial to the reported total stopping curve. The stopping power of H in Ag has more than 40 different sets of measurements. However, the maximum is not experimentally well defined, as shown in Fig. 11. The latest measurements around the maximum were reported by Semrad and co-workers [48,52] more than 30 years ago. It is worth mentioning that the present total stopping values agree very well with this group of measurements.

In Figs. 12 and 13 we display the present results for the stopping power of Pt and Au for H as a function of the impact energy, from 0.1 keV to 100 MeV. For Pt in Fig. 12, our total stopping agrees well with the data at low and high energies. The stopping maximum is very sensitive in both theoretical models and experimental setups. In this case, the present results around the maximum are close to the recent data from Refs. [18,51,53], with a slight overestimation on our model. We also include here our previous results [32], which contain ten valence electrons in the FEG. We consider the present proposal of an inhomogeneous distribution function for d electrons to be more physically sound than the previous one. As in all the targets studied here, the maximum of the d curve corresponds to $v \simeq v_d$. Similarly to Pd, Pt has a small mean velocity of the d subshell. Concomitantly, the d curve in Fig. 12 has a maximum at $E \sim 100$ keV, and for higher impact energies, the curve is lower than the contribution of the deepest $1s$ to $4f$ subshell. It is worth mentioning that the SLPA-LM results for these deep shells support the excellent

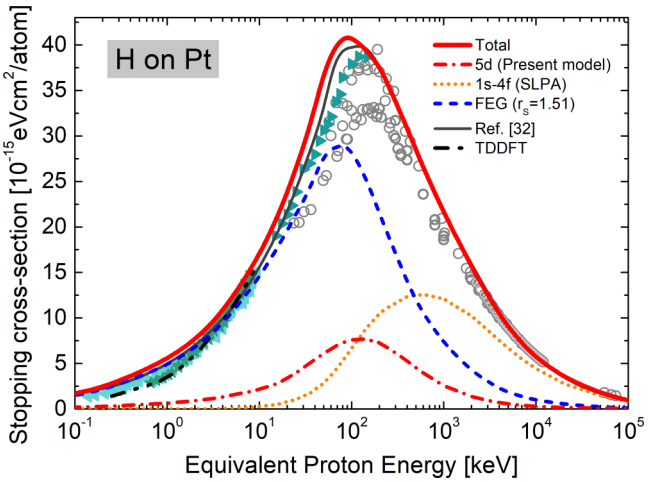

FIG. 12. Stopping cross section of Pt for H as a function of the impact energy. Curves are the same as in Fig. 8, with the TDDFT curve from [25]. Symbols are the same as in Fig. 6, as well as ◯ denoting the experimental data in [28].

agreement at high energies. Unfortunately, for Pt, TDDFT [25] is available only at low energies. Recent TDDFT Penn results [54] for H in Si manage to cover a wide energy range. The extension of this model to the present targets would be interesting.

The case of H in Au is rather singular. This system has the most significant number of stopping power measurements: 72 data sets and 1163 data points [28,29]. This amount of data also implies having the largest experimental dispersion, as clearly noted in Fig. 13. As in the other cases, the present results have overall good agreement with the experimental values in a very extensive energy range. It is fair to say that Au, with 79 electrons, is the most complex case considered here, and the response of all the 79 electrons has been considered. The agreement at high energies is very good and the agreement at low and intermediate energies is good only with some data sets. The present total stopping overestimates the most recent data at low energies [9] and around the maximum [18], being closer to previous measurements [45]. The MELF-GOS values by de Vera *et al.* [20] are also displayed in Fig. 13. These calculations show very good agreement around the stopping maximum and above and converge to the present results for impact energies higher than 200 keV.

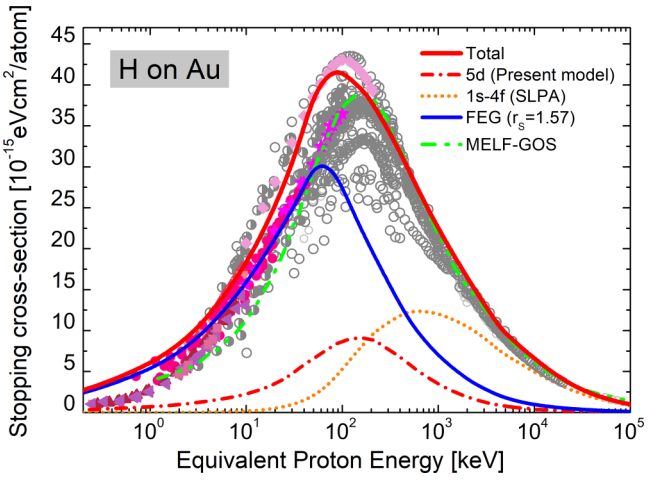

FIG. 13. Stopping cross section of Au for H as a function of the impact energy. Curves are the same as in Fig. 10, with the MELF-GOS curve from [20]. Symbols are the same as in Fig. 7, as well as ◯ denoting the experimental data in [28].

IV. CONCLUSION

In this work we introduced a nonperturbative theoretical model to deal with the contribution of the d electrons to the stopping power. The present proposal is based on the inhomogeneous momentum distribution function of the d subshell. We found it especially suitable for the later transition metals whose d electrons have minimal binding energies. This feature allows a partial promotion to the conduction band, which causes the remaining bound electrons to contribute to the energy loss at very low impact velocities.

We systematically studied the stopping power for the transition metals of groups 10 and 11: Ni, Cu, Pd, Ag, Pt, and Au. We examined the low-energy dependence with the ion velocity of the energy loss and the total stopping power in an extended energy region. In the former, we obtained that the d contribution is relevant at very low impact velocities. The sharp change of slope mentioned in experimental works is not found; instead, a soft nonlinearity coherent with an inhomogeneous momentum distribution function is obtained. The extension to higher energies allowed us to show that the present model has a maximum contribution at an impact velocity similar to the mean velocity of the d electrons.

The agreement between our total stopping power and the experimental data at low energies is very good for group 10 transition metals. For the group 11 targets, the spread of data at low energies is large. Our results agree with some of the experimental values. We do not rule out certain overestimations at very low impact velocities due to possible missing features, such as minimum energy of the remaining bound d electrons. The comparison with available TDDFT at low energies is good and has allowed us to validate and critically evaluate the present results.

We extended the description of the total stopping in a large energy region by including all the electronic contributions, from the FEG up to the deepest 1s electrons. To that end, we combined the present nonperturbative model for the d-subshell contribution with other approaches for the FEG and for the inner shells. In this way, we provided a coherent theoretical method capable of describing the stopping power of the later transition metals from the very-low- to the high-, yet not relativistic, energy region. The whole picture given by the six cases analyzed here is promising.

ACKNOWLEDGMENTS

We acknowledge Dr. Jorge Miraglia for his enlightened discussions about this work. The following institutions of Argentina financially support this research: the Consejo Nacional de Investigaciones científicas y Técnicas (CONICET) by the Project PIP11220200102421CO, the Agencia Nacional de Promoción Científica y Tecnológica (ANPCyT) by the Project PICT-2020-SERIE A-01931.

APPENDIX: MOMENTUM DISTRIBUTION CALCULATIONS

In the present model, we propose an inhomogeneous momentum distribution function $f(p)$ for the d electrons given by

$$f_{nl}(p) = \frac{(2\pi)^3}{2} |\Phi_{nl}(\vec{p})|^2, \tag{A1}$$

where $\Phi_{nl}(p)$ is the Fourier transform of the radial wave function $\phi_{nl}(r)$ [or $\phi_{nl\pm}(\vec{r}\,)$ for the relativistic wave functions], with nl the quantum numbers and in this case $l = 2$. We express the radial wave function in terms of Slater functions to have an analytical expression for $\Phi_{nl}(p)$.

The radial wave function can be expanded in a Slater function as

$$\phi_{nl}(r) = \sum_j C_j R_{n_j l}(r), \tag{A2}$$

where

$$R_{n_j l}(r) = N_j r^{(n_j-1)} e^{-\zeta_j r}, \tag{A3}$$

with N_j given by

$$N_j = (2\zeta_j)^{n_j+1/2}/[(2n_j)!]^{1/2} \tag{A4}$$

The parameters ζ_j, C_j, and n_j are the coefficients of the Slater expansion and the main quantum number, respectively.

The Fourier transform of the wave function expressed in Eqs. (A2)–(A4) is

$$\begin{aligned}\Phi_{nl}(\bar{p}) &= \frac{1}{(2\pi)^{3/2}} \int \phi_{nl}(r) e^{i\vec{p}\cdot\vec{r}} d\bar{r} \\ &= \sum_j A_j \int r^{(n_j-1)} e^{-\zeta_{n_j l} r - i\vec{p}\cdot\vec{r}} d\bar{r},\end{aligned} \tag{A5}$$

where $A_j = N_j C_j/(2\pi)^{3/2}$. We make use of the Flannery-Levy [40] solution of this integral given by

$$\int_0^\infty r^\beta e^{-\alpha r + i\vec{p}\cdot\vec{r}} d\bar{r} = 4\pi i^l (\beta - l + 1)! F_l(p), \tag{A6}$$

where

$$F_l(p) = \sum_{q=1}^{q_{\max}} b_q \alpha^{s-l-q} \frac{p^l}{(\alpha^2 + p^2)^s}, \tag{A7}$$

with $s = \beta + 3 - q$, $q_{\max} = (\beta - l + 2)/2$ or $(\beta - l + 3)/2$ for $\beta - l$ even or odd, and

$$b_q = (-1)^{q-1} \frac{(s-1)!}{(q-1)!} \frac{2^{s-q}}{(s-l-q)!}.$$

For the case of d subshells studied here, by substituting (A6) in (A5), we obtain

$$\Phi_{nd}(p) = \sum_j (-4\pi) A_j (n-2)! F_2(p). \tag{A8}$$

Substituting Eq. (A8) in Eq. (7) and carrying out some algebraic calculations, the distribution function for the case of $3d$ electrons is

$$\begin{aligned}f_{3d}(p) = \frac{(2\pi)^3}{2} |\Phi_{32}(p)|^2 &= \frac{(2\pi)^3}{2} \frac{N_e}{4\pi} \frac{3^2 \times 2^9}{\pi} \\ &\times \sum_{i=1}^{5} \sum_{j=1}^{5} \frac{A_i A_j \zeta_i \zeta_j p^4}{\left(\zeta_i^2 + p^2\right)^4 \left(\zeta_j^2 + p^2\right)^4},\end{aligned} \tag{A9}$$

where $N_e/4\pi$ comes from the normalization of the wave function to the number of $3d$ electrons. Substituting (A9) in the integral $I(v_r)$ of Eq. (6), we obtain

$$I(v_r) = \frac{(2\pi)^3}{2} \frac{N_e}{4\pi} \frac{3^2 \times 2^9}{\pi} \sum_{i=1}^{5} \sum_{j=1}^{5} A_i A_j \zeta_i \zeta_j G(v_r), \tag{A10}$$

where

$$G(v_r) = (v_r + v^2) g_5(\zeta_i, \zeta_j, v_r) - g_7(\zeta_i, \zeta_j, v_r), \tag{A11}$$

with

$$g_5(\zeta_i, \zeta_j, v_r) = \int_{|v_r - v|}^{v_r + v} \frac{p^5 dp}{\left(\zeta_i^2 + p^2\right)^4 \left(\zeta_j^2 + p^2\right)^4} \tag{A12}$$

and

$$g_7(\zeta_i, \zeta_j, p) = \int_{|v_r - v|}^{v_r + v} \frac{p^7 dp}{\left(\zeta_i^2 + p^2\right)^4 \left(\zeta_j^2 + p^2\right)^4}. \tag{A13}$$

The integrals in Eqs. (A12) and (A13) are analytical, so Eq. (6) can be included in Eq. (5). Numerical integration is also possible, and in fact we have checked both.

Analogously, the distributions $f_{4d}(p)$ and $f_{5d}(p)$ were obtained. The algebra follows the same steps, although the calculation is heavier in these cases due to the number of terms to consider. The expression of $f_{3d}(p)$ given by Eq. (A9) can be generalized for all and we obtain $f_{nd}(p)$ as a linear combination of the functions $h(a, b, i, j)$ of the type

$$h(a, b, i, j, p) = \frac{p^4}{(a^2 + p^2)^i (b^2 + p^2)^j}, \tag{A14}$$

with $i = j = 4$ for the $3d$ subshell, $i = 4 - 5$ and $j = 4 - 5$ for the $4d$, and $i = 4 - 6$ and $j = 4 - 6$ for the $5d$ subshell. The integrals $I(v_r)$ of Eq. (6) could be calculated analytically, but in the two latter cases, it was done numerically.

[1] G. J. Leigh (ed.), *Principles of Chemical Nomenclature: A Guide to IUPAC Recommendations* (RSC, Cambridge, 2011).

[2] G. P. Williams, *Electron Binding Energies of the Elements*, 95th ed. (CRC, Boca Raton, 2014), Chap. 10, pp. 200–205.

[3] C. C. Montanari and J. E. Miraglia, Nucl. Instrum. Methods Phys. Res. Sect. B **460**, 27 (2019).

[4] C. C. Montanari and J. E. Miraglia, Phys. Rev. A **96**, 012707 (2017).

[5] J. E. Valdés, P. Vargas, and V. A. Esaulov, Radiat. Eff. Defects Solids **171**, 60 (2016).

[6] S. N. Markin, D. Primetzhofer, M. Spitz, and P. Bauer, Phys. Rev. B **80**, 205105 (2009).

[7] E. D. Cantero, G. H. Lantschner, J. C. Eckardt, and N. R. Arista, Phys. Rev. A **80**, 032904 (2009).

[8] J. E. Valdés, J. C. Eckardt, G. H. Lantschner, and N. R. Arista, Phys. Rev. A **49**, 1083 (1994).

[9] S. N. Markin, D. Primetzhofer, S. Prusa, M. Brunmayr, G. Kowarik, F. Aumayr, and P. Bauer, Phys. Rev. B **78**, 195122 (2008).

[10] D. Roth, C. Celedon, D. Goebl, E. Sanchez, B. Bruckner, R. Steinberger, J. Guimpel, N. Arista, and P. Bauer, Nucl. Instrum. Methods Phys. Res. Sect. B **437**, 1 (2018).

[11] J. E. Valdés, G. Tamayo, G. Lantschner, J. Eckardt, and N. Arista, Nucl. Instrum. Methods Phys. Res. Sect. B **73**, 313 (1993).

[12] D. Goebl, D. Roth, and P. Bauer, Phys. Rev. A **87**, 062903 (2013).

[13] C. Celedón, E. A. Sánchez, M. S. Moreno, N. R. Arista, J. D. Uribe, M. Mery, J. E. Valdés, and P. Vargas, Phys. Rev. A **88**, 012903 (2013).

[14] C. E. Celedón, E. A. Sánchez, L. S. Alarcón, J. Guimpel, A. Cortés, P. Vargas, and N. R. Arista, Nucl. Instrum. Methods Phys. Res. Sect. B **360**, 103 (2015).

[15] S. P. Møller, A. Csete, T. Ichioka, H. Knudsen, U. I. Uggerhøj, and H. H. Andersen, Phys. Rev. Lett. **88**, 193201 (2002).

[16] B. Bruckner, D. Roth, D. Goebl, P. Bauer, and D. Primetzhofer, Nucl. Instrum. Methods Phys. Res. Sect. B **423**, 82 (2018).

[17] J. E. Valdés, C. Agurto, F. Ortega, P. Vargas, R. Labbé, and N. Arista, Nucl. Instrum. Methods Phys. Res. Sect. B **164–165**, 268 (2000).

[18] D. Primetzhofer, Phys. Rev. B **86**, 094102 (2012).

[19] C. D. Denton, I. Abril, J. C. Moreno-Marín, S. Heredia-Avalos, and R. Garcia-Molina, Phys. Status Solidi B **245**, 1498 (2008).

[20] P. de Vera, I. Abril, and R. Garcia-Molina, Front. Mater. **10**, 1249517 (2023).

[21] M. A. Zeb, J. Kohanoff, D. Sánchez-Portal, A. Arnau, J. I. Juaristi, and E. Artacho, Phys. Rev. Lett. **108**, 225504 (2012).

[22] E. E. Quashie, B. C. Saha, and A. A. Correa, Phys. Rev. B **94**, 155403 (2016).

[23] E. E. Quashie and A. A. Correa, Phys. Rev. B **98**, 235122 (2018).

[24] S.-M. Li, F. Mao, X.-D. Zhao, W.-Q. Jin, W.-Q. Zuo, B.-S. Li, F. Wang, and F.-S. Zhang, Phys. Rev. B **106**, 014103 (2022).

[25] C.-K. Li, X. Guo, J.-M. Xue, and F.-S. Zhang, Phys. Rev. A **107**, 052814 (2023).

[26] X.-D. Zhao, F. Mao, and H. Deng, Phys. Rev. A **109**, 032807 (2024).

[27] E. Runge and E. K. U. Gross, Phys. Rev. Lett. **52**, 997 (1984).

[28] Electronic Stopping Power of Matter for Ions, https://www-nds.iaea.org/stopping/.

[29] C. C. Montanari, P. Dimitriou, L. Marian, A. M. P. Mendez, J. P. Peralta, and F. Bivort-Haiek, Nucl. Instrum. Methods Phys. Res. Sect. B **551**, 165336 (2024).

[30] N. D. Mermin, Phys. Rev. B **1**, 2362 (1970).

[31] C. C. Montanari and J. E. Miraglia, in *Advances in Quantum Chemistry: Theory of Heavy Ion Collision Physics in Hadron Therapy*, edited by D. Belkic (Elsevier, New York, 2013), Vol. 2, Chap. 7, pp. 165–201.

[32] J. P. Peralta, M. Fiori, A. M. P. Mendez, and C. C. Montanari, Phys. Rev. A **105**, 062814 (2022).

[33] I. Nagy and A. Bergara, Nucl. Instrum. Methods Phys. Res. Sect. B **115**, 58 (1996).

[34] N. P. Wang, I. Nagy, and P. M. Echenique, Phys. Rev. B **58**, 2357 (1998).

[35] F. Salvat, J. Fernández-Varea, and W. Williamson Jr., Comput. Phys. Commun. **90**, 151 (1995).

[36] C. Bunge, J. Barrientos, and A. Bunge, At. Data Nucl. Data Tables **53**, 113 (1993).

[37] M. Klapisch, J. L. Schwob, B. S. Fraenkel, and J. Oreg, J. Opt. Soc. Am. **67**, 148 (1977).

[38] A. Bar-Shalom, M. Klapisch, and J. Oreg, J. Quant. Spectrosc. Radiat. Transfer **71**, 169 (2001).

[39] A. M. P. Mendez, C. C. Montanari, and D. M. Mitnik, Nucl. Instrum. Methods Phys. Res. Sect. B **460**, 114 (2019).

[40] M. R. Flannery and H. Levy II, J. Chem. Phys. **50**, 2938 (1969).

[41] W. S. M. Werner, K. Glantschnig, and C. Ambrosch-Draxl, J. Phys. Chem. Ref. Data **38**, 1013 (2009).

[42] Z. Lin, L. V. Zhigilei, and V. Celli, Phys. Rev. B **77**, 075133 (2008).

[43] A. Nomura and S. Kiyono, J. Phys. D **8**, 1551 (1975).

[44] K. Morita, H. Akimune, and T. Suita, J. Phys. Soc. Jpn. **25**, 1525 (1968).

[45] G. Martínez-Tamayo, J. C. Eckardt, G. H. Lantschner, and N. R. Arista, Phys. Rev. A **54**, 3131 (1996).

[46] C. C. Montanari, J. E. Miraglia, and N. R. Arista, Phys. Rev. A **62**, 052902 (2000).

[47] J. P. Peralta, A. M. P. Mendez, D. M. Mitnik, and C. C. Montanari, Phys. Rev. A **107**, 052809 (2023).

[48] D. Semrad, P. Mertens, and P. Bauer, Nucl. Instrum. Methods Phys. Res. Sect. B **15**, 86 (1986).

[49] J. C. Eckardt, Phys. Rev. A **18**, 426 (1978).

[50] M. V. Moro, P. Bauer, and D. Primetzhofer, Phys. Rev. A **102**, 022808 (2020).

[51] F. Cheng, P. de Vera, and R. Garcia-Molina, Phys. Rev. B **110**, 235134 (2024).

[52] C. Eppacher and D. Semrad, Nucl. Instrum. Methods Phys. Res. Sect. B **69**, 33 (1992).

[53] F. F. Selau, H. Trombini, G. G. Marmitt, A. M. H. de Andrade, J. Morais, P. L. Grande, I. Alencar, M. Vos, and R. Heller, Phys. Rev. A **102**, 032812 (2020).

[54] F. Matias, P. L. Grande, N. E. Koval, J. M. B. Shorto, T. F. Silva, and N. R. Arista, J. Chem. Phys. **161**, 064310 (2024).